First down converter multilayers integration in an industrial Si solar cell process

Lucile Dumont, Julien Cardin, Christophe Labbé, Cédric Frilay,
Pierre-Matthieu Anglade, Ing-song Yu, Maxime Vallet, Patrizio Benzo, Marzia
Carrada, Didier Stiévenard, et al.

First down converter multilayers integration in an industrial Si solar cell process

Lucile Dumont[1] | **Julien Cardin[1]** (iD) | **Christophe Labbé[1]** | **Cédric Frilay[1]** |
Pierre-Matthieu Anglade[1] | **Ing-Song Yu[2]** | **Maxime Vallet[3]** | **Patrick Benzo[3]** |
Marzia Carrada[3] | **Didier Stiévenard[4]** (iD) | **Hocine Merabet[5]** | **Fabrice Gourbilleau[1]** (iD)

[1] Normandie Univ., ENSICAEN, UNICAEN, CEA, CNRS, CIMAP, Caen Cedex 4, France

[2] Department of Materials Science and Engineering, National Dong Hwa University, Hualien, Taiwan

[3] CEMES/CNRS, Université de Toulouse, Toulouse Cedex 4, France

[4] IEMN, UMR8520, Université de Lille1, Villeneuve d'Ascq Cedex, France

[5] Department of Mathematics, Statistics, and Physics, College of Arts and Sciences, Qatar University, Doha, Qatar

Correspondence
Fabrice Gourbilleau, Normandie Univ., ENSICAEN, UNICAEN, CEA, CNRS, CIMAP, 6 Boulevard Maréchal Juin 14050 Caen Cedex 4, France.
Email: fabrice.gourbilleau@ensicaen.fr

Abstract

Down converter $SiN_x:Yb^{3+}/SiN_x:Tb^{3+}$ multilayers are deposited by reactive magnetron cosputtering with the objective of optimizing the interaction distance between Tb^{3+} and Yb^{3+} ions to favor a better light management in Si solar cells. Those Si-based multilayers are developed to be compatible with the Si photovoltaic technology. The deposition parameters are optimized to enhance the emission of the Yb^{3+} ions in the IR region. The emission efficiency of such multilayer structure is compared with a mixed *RE* $SiN_x:Tb^{3+}-Yb^{3+}$ layer evidencing a gain resulting from a better management of the Tb^{3+} and Yb^{3+} ions distance. At the end, we integrate the growth of such a multilayer in an industrial Si solar cell process and demonstrate the existence of a frequency conversion effect that is promising for the future increase of the Si solar cell efficiency.

KEYWORDS

down converter, rare earth ions, Si solar cell efficiency, SiN_x, Tb-Yb

1 | INTRODUCTION

The limitation of global average temperature increase to 2°C agreed by the international community at the COP21 Paris's meeting strengthens the need of developing carbon free sustainable energies. To reach this goal, the use of sustainable energy sources, particularly solar energy, has to be optimized while their running cost has to be decreased. In this context, continuous improvements have been done on silicon solar cell that is actually the most used nowadays solar power generation. Thus, a typical conversion efficiency of about 20% is industrially validated and more recently a value as high as over 26%[1] has been achieved in lab. Thus, increasing its efficiency while keeping a low cost process is one of the goals of the silicon-photovoltaic (*Si-PV*) industry to continuously decrease the cost of the power generation and thus increase its competitiveness. The limited efficiency of *Si-PV* comes principally from thermalization of photogenerated minority carriers.[2] Hence, the energy excess of these photogenerated excitons with respect to the Si solar cell (*Si-SC*) bandgap energy is released into the matrix. As a result, besides a limited

energy conversion, such a process may increase the cell temperature and therefore reduce the efficiency of the cell. For example, an increase of 1°C above 25°C leads to a decrease of the *SC* efficiency by around 0.65%[3-5] and results in its faster aging. Several ways to improve the *SC* efficiency[6] are thus investigated such as tandem cells,[7,8] surface *texturing*,[9,10] antireflective layer,[11-13] or frequency conversion layer.[2,14-20] In that respect, down conversion (*DC*) answers the thermalization issue by converting high energy photons to a greater number of lower energy photons with energies close to the *Si-SC* gap. Many systems using a couple of rare earth (*RE*) ions, such as $Pr^{3+}-Yb^{3+}$,[21-23] $Tb^{3+}-Yb^{3+}$,[24-27] and $Ce^{3+}-Yb^{3+}$,[28,29] have been studied for the DC approach. The major drawbacks of those different developed systems are the use of a non–Si-compatible process due to the nature of the host matrix and/or the low absorption cross section of the *RE* ions that limits their excitability in the solar spectrum range.[15,30] To overcome this problem, a *Si-PV* compatible host matrix containing sensitizers has been developed in our group taking into account that such a host matrix should have good antireflective properties to be used as antireflection coating (*ARC*).[31]

The aim of this paper is to study the development of down-conversion layers whose fabrication process is fully compatible with the *Si-PV* industry one. To achieve this goal, the silicon nitride SiN$_x$ host matrix doped with terbium and ytterbium ions was chosen. The obtained system absorbs a *UV* photon with an energy twice higher than the Si bandgap and emits two *IR* photons with an energy just above it. Thus, the number of photogenerated carriers having an energy that matches with the *Si-SC* bandgap is maximized at the expense of high-energy carriers.

A previous study of the SiN$_x$:Tb^{3+}-Yb^{3+} system in a monolayer approach has demonstrated a down-conversion process occurring in a four steps process: (1) the matrix absorbs *UV* photons, (2) the excited sensitizers present in the host matrix transfer their energy to high energy levels of Tb^{3+} ions that de-excites to its $^5D_4$ energy level, (3) Tb^{3+} ions transfer cooperatively the energy from their $^5D_4$ energy level to the Yb^{3+} ions $^2F_{5/2}$ energy level from which the *IR* photons around 990 nm are emitted, and (4) extraction of the IR photons to the underlying solar cell.[32] For the two first points, we have recently evidenced that this is the defect states related energy levels in the bandgap of the SiN$_x$ host matrix such as silicon-related defects, for example, which absorb the energetic photons and transfer the energy to the resonant energy levels of Tb^{3+} ($^5G_6$, $^5D_3$-$^7F_6$, $^5D_3$-$^7F_4$, $^5D_4$-$^7F_6$). This dipole-dipole interaction process is at the origin of the excitation of Tb^{3+} ions even under nonresonant wavelength.[33]

Such SiN$_x$:Tb^{3+}-Yb^{3+} layer showing a high Yb^{3+} photoluminescence (*PL*) peak intensity was obtained and found to transmit more photons to the Si substrate (considered as the solar cell) than a previous system studied SiO$_x$N$_y$:Tb^{3+}-Yb^{3+} [31]. This improvement was mainly attributed to the higher rare earth ions incorporation in the pure nitride layer without the detrimental clustering effect observed in rare earth doped sputtered oxide Si-based matrix.[32] Moreover, in the case of a cooperative energy transfer mechanism (*CET*) such as the one between Tb^{3+} and Yb^{3+} ions, the efficiency of the coupling rate between these ions is very dependent of the distance Tb^{3+}:Yb^{3+} in a one donor/two acceptors configuration. The dipole-dipole interaction rate evolves proportionally to the inverse sixth power of both donor-acceptor separation distance.[34] Consequently, the *CET* efficiency is strongly correlated to both rare earth ions concentrations.

This demonstrates the importance to manage the inter-ions distance through the concentration and film structure. For this purpose, in this work, a SiN$_x$:Yb^{3+}/SiN$_x$:Tb^{3+} multilayer is developed and optimized to favor the emission in the infrared region by monitoring Tb^{3+}:Yb^{3+} distance. Such a structure has already been investigated in similar system and has evidenced the importance of the interaction distance tuning.[35] The microstructure and optical properties of this multilayer structure are investigated. The optimized multilayer system is then deposited on an industrial Si solar cell, and its performances measured and discussed.

2 | EXPERIMENTAL

The layers were deposited on *p*-type 250-μm-thick (001) 2″ silicon substrates by reactively cosputtering Si, Tb, and Yb targets in a nitrogen-rich plasma. The optimized conditions for achieving a host matrix with the suitable characteristics have been determined in a previous work

published by Debieu et al.[36] The SiN$_x$ host matrix has been obtained by sputtering the Si target under an *RF* power (*RFP*) density fixed at 4.5 W·cm^{-2}. The plasma pressure was set at 3 mTorr with an *Ar/N$_2$* ratio fixed at 4 while the rotating substrate was heated at 200°C. The incorporation of the *RE* has been controlled by varying the *RF* power density applied on the Tb and Yb cathodes separately. For the former, *RFP$_{Tb}$* ranges from 0.45 to 3.75 W·cm^{-2} while for the latter, *RFP$_{Yb}$* density is fixed between 0.1 and 0.25 W·cm^{-2}. The deposition time of the sublayers was varied to achieve the expected thickness between 0.8 and 6.0 nm for the Tb-doped sublayers, and between 0.4 and 2.6 nm for the Yb-doped ones. After deposition, the samples were annealed using a classical thermal annealing approach (*CTA*) that consists in introducing the films in a tubular furnace at 850°C during 1 hr under a pure nitrogen flow. Fourier transform infrared (*FTIR*) measurements were performed on layers at room temperature thanks to a *Thermo Nicolet Nexus 470 II* spectrometer working in the 4000 to 400 cm^{-1} range, with a 5 cm^{-1} resolution. Ellipsometry measurements were performed to determine the complex refractive index and the thickness of the films using an *UVISEL Jobin-Yvon* ellipsometer with an incident angle of 66.2°. The experimental I_c and I_s ellipsometry spectra were recorded on a 1.5 to 5 eV range with 0.01 eV resolution. The determinations of the refractive index n and the layer thickness t have been achieved by fitting the experimental data by a dispersion law derived from the Forouhi-Bloomer model[37] for amorphous semiconductors using the *DeltaPsi2* software. Prior to the deposition of the multilayer, the average deposition rates of the Tb-doped and Yb-doped SiN$_x$ layers have been defined. The goal is to know the determination of the deposition time of each sublayer to achieve the desired sublayer thicknesses in the SiN$_x$:Yb^{3+}/SiN$_x$:Tb^{3+} multilayer structure.

Cross-sectional *TEM* samples along the [110] zone axis of the silicon substrate were prepared by focused ion beam (*FIB*) on a FEI Helios dual-beam Nanolab 600i. High angle annular dark field scanning transmission electron microscopy (*HAADF-STEM*) and the spatially resolved electron energy loss spectroscopy (*EELS*) have been carried out on a *JEOL cold-FEG JEM-ARM200F* operated at 200 kV and equipped with a probe Cs corrector and a *GATAN GIF Quantum ER* spectrometer. Electron energy loss spectroscopy (*EELS*) experiments have been performed by using a slit aperture of 2.5 mm and dispersions of 0.3 or 0.5 eV/px depending on the studied energy range.

Photoluminescence (*PL*) and photoluminescence in excitation (*PLE*) experiments were performed at room temperature on the annealed layers. Concerning the *PL* experiments, a *Crylas CW FQCW-266* laser was used as an excitation source. After dispersing the *PL* signal through a *Jobin-Yvon TRIAX180* monochromator, the emission data were recorded using a *Hamamatsu (R5108)* photomultiplier tube connected to a *FEMTO DLPCA-200* trans-impedance amplifier. The detection system was locked in with a *SR830* amplifier referenced at the excitation light beam chopped frequency. For the *PLE* experiments, a *Lot-Oriel 1 kW Xenon* lamp connected to an *OMNI300* monochromator was used as a tunable light source. After dispersing the *PL* signal through a *MSH 300 OMNI* monochromator, the emission data were recorded using a *Hamamatsu (R5108)* photomultiplier tube with trans-impedance amplification. The detection system was locked in with a *SR830* amplifier referenced at the excitation light beam chopped frequency. The *PL* and *PLE* spectra obtained were corrected by the sample's thickness and by the lamp emission intensity in the *PLE* case.

3 | RESULTS AND DISCUSSION

3.1 | Structure fabrication

As detailed in the introduction, the efficiency of the cooperative energy transfer (CET) depends on the distance between terbium and ytterbium ions. Classically, in mixed RE-layers produced by such a deposition technique, the probability of having a terbium ion close enough to two ytterbium ones is low, limiting the potential gain of such frequency conversion layers in the enhancement of the cell efficiency as reported elsewhere.[31] To investigate such a critical issue, a multilayer (ML) structure consisting in a stacking of SiN_x:Yb^{3+} and SiN_x:Tb^{3+} sublayers has been developed. The fabrication process consists in depositing first, a SiN_x:Yb^{3+} sublayer by cosputtering a Si and Yb targets using nitrogen-rich plasma under appropriate RF power densities on Si (4.5 W·cm^{-2}) and Yb (RFP_{Yb}) targets. When the thickness of the SiN_x:Yb^{3+} sublayer is reached, plasma is stopped, shutters on Yb and Si targets closed, and the chamber pumped to remove any Yb species in the chamber. The plasma is run again with the selected RF power density applied on Si (4.5 W·cm^{-2}) and Tb (RFP_{Tb}) targets. After few seconds of stabilization, both shutters are opened to deposit SiN_x:Tb^{3+} sublayer. As previously, when the thickness of the SiN_x:Tb^{3+} sublayer is obtained, plasma is stopped, shutters on Tb and Si targets closed, and the chamber pumped to remove any Tb species in the chamber. To keep a total thickness of the film lower than 100 nm, 25 stacks of the pattern formed by the couple SiN_x:Yb^{3+}/SiN_x:Tb^{3+} have been deposited. The SiN_x:Yb^{3+}/SiN_x:Tb^{3+} structure obtained begins with a SiN_x:Yb^{3+} sublayer and finishes with a SiN_x:Tb^{3+} one. It will be noted in the following as $XC25(t_{Yb}/t_{Tb})$ where t_{Yb} and t_{Tb} are the thicknesses of the Yb^{3+}-doped and Tb^{3+}-doped sublayers, respectively. Such a structure offers the possibility to tune both concentration of RE ions in each sublayer and interaction distance between Tb^{3+} and Yb^{3+}.

3.2 | Effect of the deposition parameters

3.2.1 | Ytterbium target power density, RFP$_{Yb}$

In this section, we describe the way to optimize the Yb^{3+} emission by fixing RFP_{Tb} at 1.5 W·cm^{-2} while RFP_{Yb} is varied from 0.1 to 0.25 W·cm^{-2}. After annealing at 850°C during 1 hr, the SiN_x:Yb^{3+}/SiN_x:Tb^{3+} emission properties are analyzed under a 285 nm excitation wavelength. The recorded spectra are reported on Figure 1A. Yb^{3+} emission intensity is maximum at 0.10 W·cm^{-2} and decreases with RFP_{Yb}. Note that the Si-based host matrix used here is not responsible of any sensitization of Yb^{3+} ions as shown in the left inset (Figure 1A). Yb^{3+} ions in the SiN_x-Yb^{3+} film do not present any emission under an excitation at 325 nm. Such excitation wavelength is also a nonresonant excitation line for the Tb^{3+} ions.[38] Thus, the intense Yb^{3+} emission observed in the left inset when Tb^{3+} ions are incorporated is the signature (1) of an efficient sensitization of the Tb^{3+} ions by the matrix that absorbs the light and transfers its energy to the Tb^{3+} ions; (2) of a cooperative energy transfer from the excited $^5D_4$ energy level of the Tb^{3+} ions to the surrounding Yb^{3+} excited $^2F_{5/2}$ level. In the right inset (Figure 1A), one can notice that the evolution of the PL_{Yb} intensity may also depend on the RFP_{Tb} applied. The objective of this inset is not to compare the PL intensity level with that of Figure 1 because the measurements have been done

separately. The goal is only to see the effect of changing the RFP_{Tb} parameter on Yb^{3+} PL intensity. Indeed, the increase from 0.1 to 0.15 W·cm^{-2} leads to a higher Yb^{3+} emission for the multilayer deposited with an RFP_{Yb} of 0.15 W·cm^{-2} whereas the same increase leads to a lower Yb^{3+} PL emission for a lower RFP_{Tb}. Thus, these different evolutions observed in the emission properties can be attributed to several contributions that can act separately or concomitantly: (1) the increasing incorporation of Yb^{3+} favors the disorder in the host matrix, and therefore, the presence of nonradiative defects that quench the PL; (2) a too low Tb concentration is not favorable to excite the increasing number of Yb^{3+}; (3) a decrease of Yb^{3+}-Yb^{3+} distance favors the energy migration process[39] as observed previously in similar mixed RE-doped thin films.[32] Considering the results achieved here, the optimum value of RFP_{Yb} is taken at 0.15 W·cm^{-2}.

3.2.2 | Terbium target power density, RFP$_{Tb}$

The optimal value of the RFP_{Yb} determined above (RFP_{Yb} = 0.15 W·cm^{-2}) has been used, and the Tb RF power density has been varied between 0.45 to 3.0 W·cm^{-2} for determining the optimal RFP_{Tb}. The corresponding PL spectra recorded under a 285 nm excitation wavelength are reported in Figure 1B. One can notice a continuous increase of the Yb^{3+} emission intensity with RFP_{Tb}. This evolution is attributed to an increasing incorporation of Tb^{3+} ions in SiN_x-Tb^{3+} sublayer with the RF power density applied on the Tb target. It leads to the decrease of the Tb^{3+}:Yb^{3+} distance and thus favors the energy transfer between these two rare earth ions. For achieving a finer optimal value of RFP_{Tb}, a second run of depositions has been carried out, always keeping the RFP_{Yb} at the same value, but varying the RFP_{Tb} from 2.7 to 3.75 W·cm^{-2}. The maximum Yb^{3+} PL intensity recorded is reported in the inset of Figure 1B as a function of RFP_{Tb}. The emission of Yb^{3+} ions increases with RFP_{Tb} up to 2.85 W·cm^{-2} before decreasing for higher values. Such a decrease is attributed to either the increase of nonradiative centers due to the increasing number of RE ions in the host matrix and/or to the decreasing Tb^{3+}-Tb^{3+} distance that may favor the energy migration process[39] as mentioned above. Thus, the optimal value for RFP_{Tb} is found to be 2.85 W·cm^{-2}. Figure 1C reports FTIR spectra recorded on as-grown $XC25(1.2/2.6)$ layers under 65° incidence. For clarity, only some selected spectra are reported. One can notice that the increase of RFP_{Tb} leads to the decrease of both LO and TO vibration modes of Si—N bonds. The absence of vibration modes peaking at around 1080 and 1250 cm^{-1} attests of the absence of any oxygen-based compound as previously observed in similar host matrix.[36,40] The analysis of the Figure 1C reveals a decrease of the Si—N bond quantity with RFP_{Tb} because all the multilayers produced here have the same total thickness.

The evolution of the refractive index at 1.95 eV with RFP_{Tb} is reported in the inset of Figure 1C and shows an increase with the RF power density applied on the Tb target. This is a signature of an increase of [Tb] incorporation and/or [Si] excess in the SiN_x host matrix. To get more details on this specific point, we have compared the x = [N]/[Si] value deduced from the refractive index (red star) or the LO position (red circle). For the former, assuming that n_{SiNx} is a bonding-density-weighted linear combination of n_{Si3N4} and n_{Si}, we have used the empirical law proposed by Bustarret et al[41] in the case of SiN_x:H films modified by Debieu et al.[36] Such an empirical approach is in agreement with the law proposed by Makino,[42] assuming that our
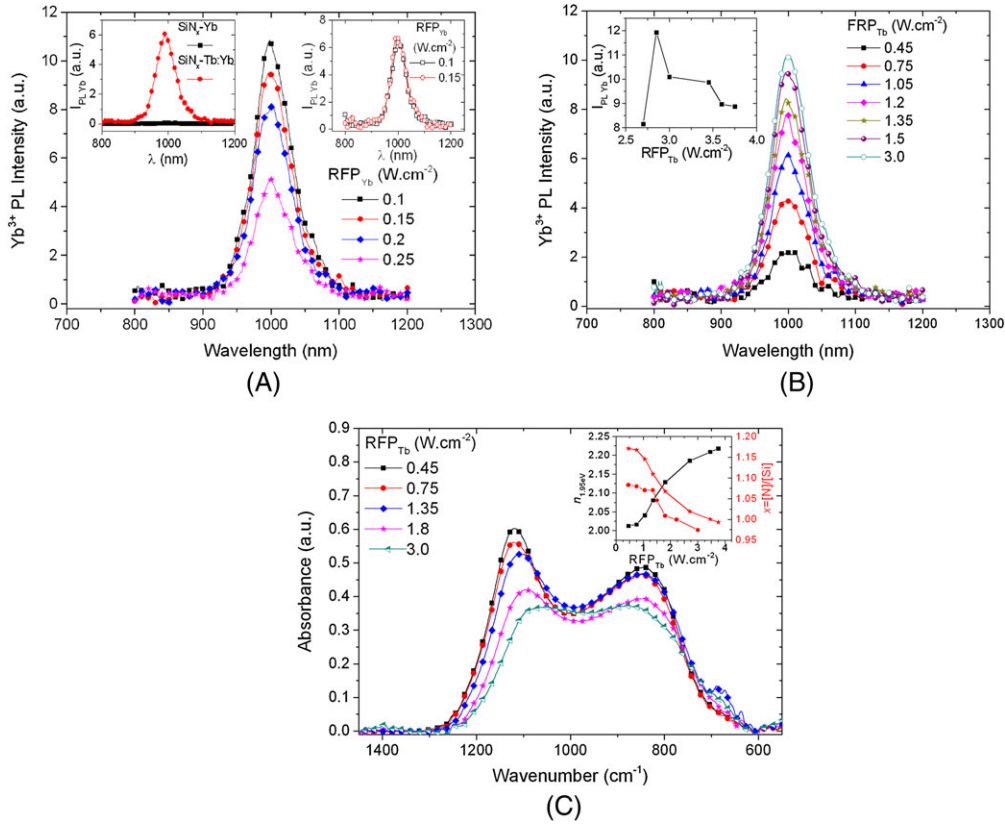
FIGURE 1 A, Yb^{3+} photoluminescence spectra of the $SiN_x:Yb^{3+}/SiN_x:Tb^{3+}$ multilayer for a λ_{exc} of 285 nm and a [600-750] grating, for different RFP_{Yb} ranging from 0.1 to 0.25 W·cm^{-2}. The MLs have been grown with an RFP_{Tb} fixed at 1.5 W·cm^{-2}. In the left inset is reported Yb^{3+} PL intensity comparison of a typical SiN_x host matrix doped with Yb^{3+} ions or $Tb^{3+}:Yb^{3+}$ couple under a λ_{exc} of 325 nm. In the right inset is reported Yb^{3+} PL spectra of $SiN_x:Yb^{3+}/SiN_x:Tb^{3+}$ MLs deposited with an RFP_{Tb} fixed at 1.8 W·cm^{-2}. B, PL spectra of $SiN_x:Yb^{3+}/SiN_x:Tb^{3+}$ MLs for a λ_{exc} of 285 nm and a [600-750] grating, for different RFP_{Tb} ranging from 0.45 to 3.0 W·cm^{-2}. In the inset is displayed the evolution of the Yb^{3+} PL intensity at 990 nm as a function of RFP_{Tb} in the 2.7-3.75 W·cm^{-2} range. The MLs have been grown with an RFP_{Yb} fixed at 0.15 W·cm^{-2}. The Yb- and Tb-doped sublayer thicknesses have been fixed at 1.2 and 2.6 nm, respectively. C, FTIR spectra of $SiN_x:Yb^{3+}/SiN_x:Tb^{3+}$ MLs recorded under Brewster incidence, for different RFP_{Tb} ranging from 0.45 to 3.0 W·cm^{-2}. In the inset is displayed the evolution of the refractive index (black curve, left y axe) and the $x = [N]/[Si]$ value (red curves, right y axe) as a function of RFP_{Tb}. The $x = [N]/[Si]$ value is deduced from the refractive index value (red star) or the LO position (red circle). The MLs have been grown with an RFP_{Yb} fixed at 0.15 W·cm^{-2}. The Yb- and Tb-doped sublayer thicknesses have been fixed at 1.2 and 2.6 nm, respectively [Colour figure can be viewed at wileyonlinelibrary.com]

produced sputtering layers do not contain any hydrogen species. The result is displayed in the inset of Figure 1C (star symbol). Concerning the LO position, we have used the empirical law that links the shift of the LO peak with the value of x.[36] The deduced value of x as a function of RFP_{Tb} is reported in the inset as circle symbol. Both curves follow the same evolution evidencing an increase of the [Si] content with respect to the [N] one. The difference noticed between these curves attests that the increase of $n_{1.95eV}$ is the concomitant result of the Tb incorporation and the increase of the [Si] content with respect to the [N] one when RFP_{Tb} is increased.

3.3 | Effect of the microstructure

3.3.1 | Terbium-doped sublayer thickness, t_{Tb}

After having optimized RFP_{Tb} and RFP_{Yb}, the next step has consisted in increasing the Yb^{3+} emission by managing the interaction distance between Tb^{3+} and Yb^{3+} ions through the thickness of each sublayer. For that purpose, $XC25(3/t_{Tb})$ multilayers have been grown with RFP_{Tb} and

RFP_{Yb} fixed at 2.85 and 0.15 W·cm^{-2}, respectively. The corresponding PL spectra recorded under a 285 nm excitation line are reported in Figure 2A. One can notice a jump of the emission at 990 nm when t_{Tb} increases from 0.8 to 1.5 nm before dropping down for higher sublayer thicknesses. The maximum emission is obtained for t_{Tb} = 1.5 nm. This is the evidence that the monitoring of the sublayer thickness is a way to optimize the interaction between both rare earth ions. Tb^{3+} ions incorporated for higher value of t_{Tb} do not participate to the cooperative energy transfer with Yb^{3+} ones, and may even have a detrimental effect because the PL intensity in Figure 2A decreases while it should be constant. This feature may underline an effect of the interfaces between each sublayer in the repartition of the rare earth ions. Consequently, the Tb-doped sublayer thickness will be fixed for the next step to 1.5 nm.

3.3.2 | Ytterbium-doped sublayer thickness, t_{Yb}

We have then determined the optimal thickness of the sublayer containing Yb^{3+} ions by applying the same procedure, fixing the Tb-doped sublayer thickness—t_{Tb}—at 1.5 nm. $XC25(t_{Yb}/1.5)$ multilayers have been
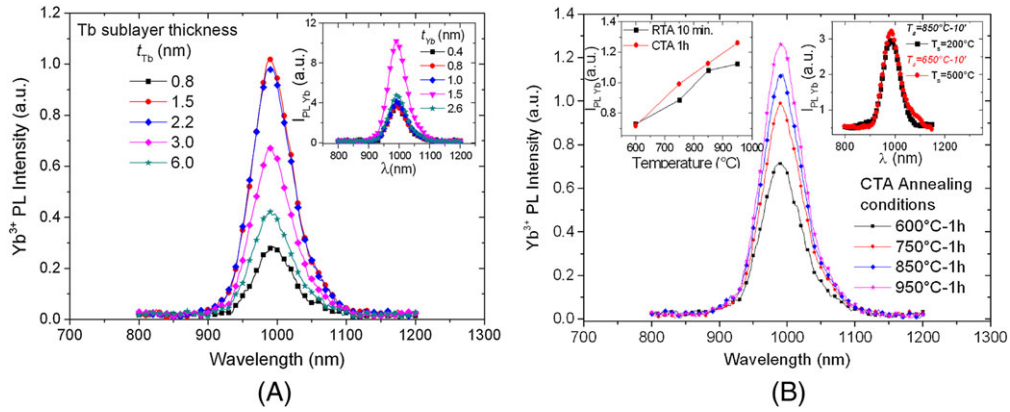
FIGURE 2 A, Photoluminescence spectra of $XC25(3/t_{Tb})$ multilayers as a function of Tb-doped sublayer thickness, t_{Tb}. The inset displays the *PL* spectra of $XC25(t_{Yb}/1.5)$ *MLs* for different Yb-doped sublayer thicknesses, t_{Yb}. The $SiN_x:Yb^{3+}/SiN_x:Tb^{3+}$ *MLs* have been annealed at 850°C during 1 hr. B, *PL* spectra of $XC25(1.5/1.5)$ *MLs* for different annealing temperatures. In the left inset: Evolution of the *PL* emission of the Yb^{3+} ion recorded at 990 nm for *RTA* and *CTA* approaches in the same range of temperatures. In the right inset: *PL* spectra of $XC25(1.5/1.5)$ *MLs* deposited at 200°C and 500°C and annealed at 850°C or 650°C, respectively, during 10 min. The excitation wavelength is fixed at 285 nm and the grating used is the [600-750] one [Colour figure can be viewed at wileyonlinelibrary.com]

grown with RFP_{Tb} and RFP_{Yb} fixed at 2.85 and 0.15 W·cm^{-2}, respectively. After annealing at 850°C during 1 hr, the emission properties in the near infrared region have been investigated using a 285 nm excitation wavelength (inset of Figure 2A). The Yb^{3+} *PL* intensity increases with t_{Yb}, to reach its maximum when Yb sublayer thickness reaches 1.5 nm and then decreases for higher thicknesses. Considering the multilayer structure, an Yb^{3+} ion can be excited from both Tb-doped surrounding sublayers. Thus, in the light of the evolution of the *PL* intensity, the optimized interaction distance between Tb^{3+} and Yb^{3+} ions should be lower than 0.8 nm (half of the Tb sublayer thickness allowing to a Tb^{3+} ion to interact with one Yb^{3+} ion in the closed sublayer).

In conclusion, for our multilayers system, the optimized structure has been achieved for a substrate temperature, RFP_{Tb} and RFP_{Yb} fixed at 200°C, 2.85 and 0.15 W·cm^{-2}, respectively. The best optical properties have been obtained for thicknesses of both sublayers fixed at 1.5 nm.

3.3.3 | Effect of the annealing treatment

The effect of annealing conditions on the optimized $XC25(1.5/1.5)$ multilayer structure has been studied. For the purpose different approaches have been considered in order to determine the optimum conditions for solar applications. Thus, rapid thermal annealing (*RTA*) and conventional thermal annealing (*CTA*) techniques have been investigated. For the former, the duration was fixed to 10 min while for the latter, 1 hr was applied. Four different annealing temperatures have been chosen ranging from 600°C to 950°C. The resulting *PL* emission recorded in the near *IR* region is exhibited in Figure 2B for the *CTA* approach. This figure evidences a continuous increase of the emission of the Yb^{3+} ion with temperature. Such an evolution is the signature of a matrix reorganization with temperature that allows the recovering of the nonradiative defects and consequently promotes the rare earth ions emission. The influence on the emission intensity of the two annealing methods is presented in the left inset of Figure 2B. One can notice that the longer annealing treatment favors the emission of Yb^{3+} ions, whatever the temperature applied. For the highest temperature a saturation of the emission appears for the *RTA* method. However, such high

annealing temperature cannot be applied due to the loss of *pn* junction integrity leading to the decrease of the *SC* efficiency. To overcome this critical issue and to compensate a decrease of the annealing temperature to 650°C, *MLs* have been produced fixing the substrate temperature to 500°C instead of 200°C. After a *RTA* annealing at 650°C during 10 min, the emission of Yb^{3+} ions is a little bit higher than the *ML* deposited at 200°C and annealed at 850°C during the same time (right inset Figure 2B). This new process could be promising for the future step of deposition on a Si solar cell and requires deeper analyses on the consequence of the performances of the solar cell. For the purpose of this paper and the study described in Section 3.7, we will keep the deposition of the *DC* layer at 200°C coupled with an annealing at 650°C during 10 min that offers anyway a safe process for the integrity of the *SC* while keeping an intense *PL* emission, only 1.3 times lower than the layer annealed at 850°C during 10 min.

3.3.4 | Microstructure of the XC25(1.5/1.5) multilayer

The microstructure of the optimized system was studied by using *HAADF-STEM*. The *HAADF-STEM* mode was chosen to get a chemical contrast within the intensity of images and thus clearly distinguish the $SiN_x:Yb$ and $SiN_x:Tb$ sublayers. Indeed, in this mode, the scattered intensity varies with the mean atomic number Z of elements, the density of materials and/or the thickness of the TEM sample.[43,44] It means that a brighter contrast can correspond to a higher Z, a higher density and/or a thicker sample. In our case, due to the low difference in Z between Tb and Yb and considering that samples were prepared by focused ion beam, the intensity contrast is mainly due to the concentration of the *RE* ions in the SiN_x layers. Figure 3A shows a general view of the optimized multilayer system composed of 19 stacks. Different layers are clearly observed with a well-contrasted alternation of bright and dark layers suggesting a change of chemical composition. Bright and dark layers are however not perfectly straight. They rather exhibit a wavy shape. An atomically resolved *HAADF-STEM* image taken close to the SiN_x/Si interface is displayed in Figure 3B. The thickness of the TEM sample in this area was assessed at 50 nm by using *EELS*.
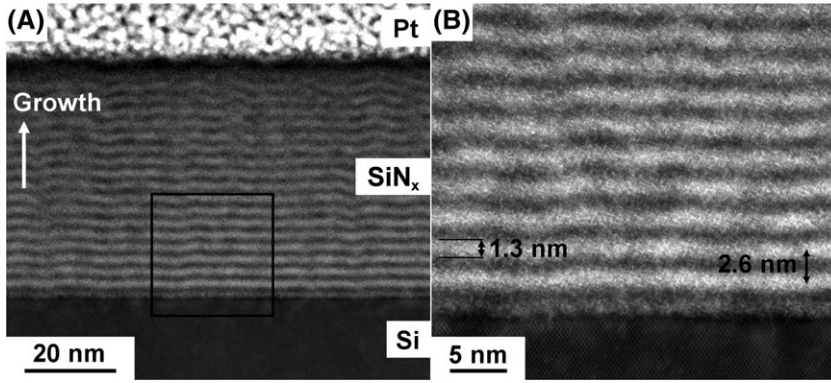
FIGURE 3 A, General view of the optimized multilayer system taken by *HAADF-STEM*. B, Atomically-resolved *HAADF-STEM* image taken close to the interface SiN$_x$/Si

Thicknesses of bright and dark sublayers were both measured on average at 1.3 ± 0.1 nm inducing a periodicity of the pattern of 2.6 nm. A detailed analysis of each sublayers does not reveal any cluster or crystalline grain at the nanometer scale. To be able to perform modeling as described in Section 3.6, the determination of the multilayers composition is an important point and required at least the [Tb]/[Yb] ratio. However, the thin thickness of each sublayer does not offer a technical possibility of determining their composition. Indeed, *RBS* technique is not able to separate these sublayers adding the fact that Tb and Yb signals are overlapping leading to a host matrix composition with too large error bars, while *SIMS* measurements required reference well-known structure produced using the same techniques. In addition, *EDX* analysis on *TEM* samples with probe of about 1 nm could be the solution but even taking all the necessary precautions, the requirement to tilt the sample to get signal coupled with the lateral resolution and the quantification in presence of light elements do not allow to get the [Tb]/[Yb] ratio. This is why we have performed *EELS* measurements to evaluate the chemical composition of SiN$_x$:*RE* sublayers. However, due to their extreme sensitivity to the electron beam that prevents long acquisition times, the chemical composition of each individual bright and dark layers could not be accurately determined. Electron energy loss spectroscopy (*EELS*) spectra were averaged over 10 nm in the growth direction in order to get significant signal for the analysis of Tb and Yb M$_{4,5}$ edges. Nevertheless, bright layers in Figure 3, which have higher *RE* concentration, were found to be rich in Tb while dark ones are rich in Yb. The average concentration of Tb and Yb in the whole SiN$_x$ layers was estimated to about 1 Tb for 6 Si and 1 Yb for 100 Si. These ratios result in a [Tb]/[Yb] ratio of about 16.

3.4 | Frequency conversion process

The *PLE* experiments have been carried out for a detection at 990 nm to determine the wavelength region contributing to the excitation

5.5 eV. Such an energy range has been previously associated to the E_c, ≡Si—Si≡σ*, ≡Si—Si≡σ, or E_v electronic transitions occurring in the SiN$_x$ matrix[32] that can match with energy levels of the Tb^{3+} ions above the $^5D_4$ such as $4f^7$ $5d$, H, F, and G levels as represented in Figure 4. After this efficient matrix-Tb^{3+} ions energy transfer, nonradiative deexcitations from the Tb^{3+} high energy levels to the $^5D_4$ one occur. Two ways are then possible: (1) the return to the ground level $^7F_6$ results in the four characteristic radiative energy transitions that can take place in the visible range or, (2) in the case of the presence of two Yb^{3+} ions in the close surrounding, a cooperative energy transfer takes place favoring the emission of two *IR* photons issued from the $^2F_{5/2}$ to $^2F_{7/2}$ Yb^{3+} transition. Note that, depending on the excitation energy, the direct excitation of the Tb^{3+} ions by the sunlight may also be considered and act in parallel of the matrix sensitization.

3.5 | Multilayer and mixed *RE*-layer comparison

We have recently demonstrated that the host matrix plays an important role in the improvement of the optical properties of frequency conversion layer.[32] As mentioned above, the structure of the layer, ie, mixed *RE*-layer or multilayer, could also be a way to optimize such properties. Figure 5 displays the *PL* spectra of an optimized mixed *RE*-layer or multilayers under a 285 nm excitation line. The comparison of the *PL* intensities evidences an increase of the emission in the multilayer structure by a factor 1.5. As previously described,[33,45] the Yb^{3+} *PL* intensity, I_{PL}, is given by the relation:

$$I_{PL} = C \left(N^* \cdot V \right) / \tau_{rad}, \tag{1}$$

where C, N^*, V, and τ_{rad} are respectively: an experimental constant, the excited state population density, the excited volume, and the Yb^{3+} radiative lifetime. The volume of interaction (77 × 10^{-6} mm^3) and the pump power density ϕ (1.9 × 10^{15} photons/cm^2) are constant during our *PL* measurements. Equation (1) can be written as follows:

$$I_{PL\,\text{Multilayer}}/I_{PL\,\text{Mixed RE}} = 1.5 = C \left(N^*_{\text{Multilayer}} \cdot V \right) \tau_{rad\,\text{Mixed RE}} / C \left(N^*_{\text{Mixed RE}} \cdot V \right) \tau_{rad\,\text{Multilayer}}. \tag{2}$$

mechanism of the Yb^{3+} ion through different energy transfer processes (Figure 4). The *PLE* spectrum reveals that Tb^{3+} ion is excited to its high energy levels via the SiN$_x$ host matrix between 3.5 and

Thus, considering that τ_{rad} is constant around 1.5 μs for both structures, on can deduce from Equation (2) the Yb^{3+} excited state ratio $N^*_{\text{Multilayer}}Yb^{3+}/N^*_{\text{Mixed RE}}Yb^{3+} = 1.5$. Taking into account that
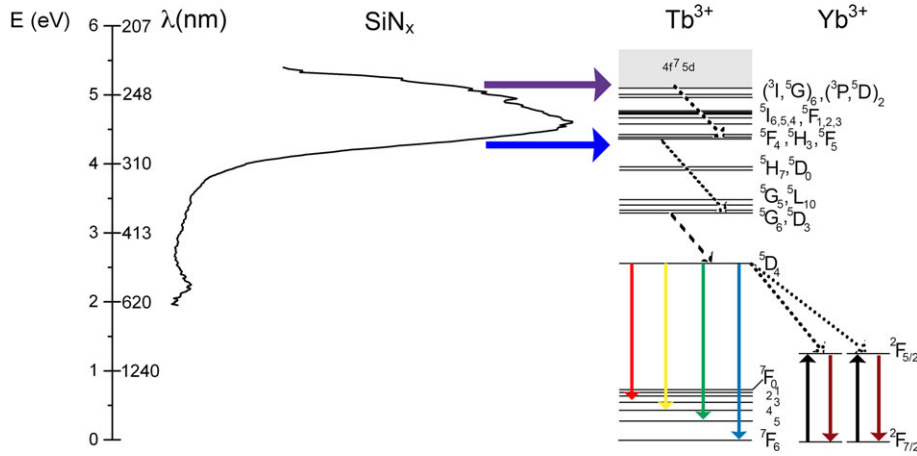
FIGURE 4 Excitation mechanism scheme for a down-conversion process. A scheme of the energy transfer between the matrix *PLE* spectrum and the energy levels of Tb^{3+} ions and thus the cooperative energy transfer between Tb^{3+} and Yb^{3+} ions with the emission of two *IR* photons at 990 nm (dark red arrows) [Colour figure can be viewed at wileyonlinelibrary.com]
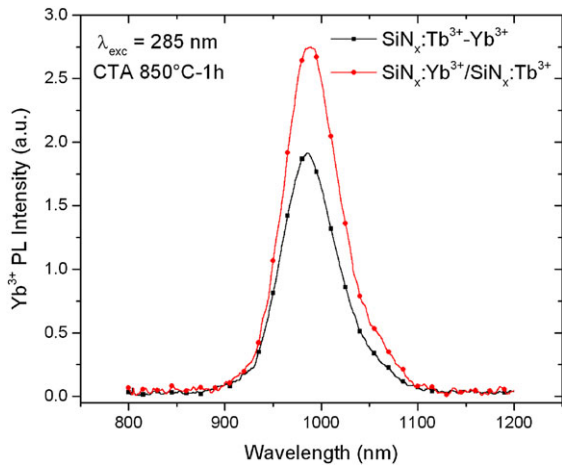

FIGURE 5 Photoluminescence spectra of a mixed *RE*-layer and multilayer structures under a 285 nm excitation line. The *PL* experiments have been carried out with a [600-750] grating [Colour figure can be viewed at wileyonlinelibrary.com]

the Yb^{3+} concentration is about 2.5 times higher in the mixed *RE*-layer than in the multilayer ([Tb]/[Yb] ratio of 6^{32} and 16 in mixed *RE*-layer and multilayers, respectively), this result is an evidence of a better Tb^{3+}-Yb^{3+} interaction distance management in the multilayer structure by comparison with the mixed *RE* film.

3.6 | Modeling

As mentioned before, the inter rare earth distance is a key parameter regarding the cooperative energy transfer (*CET*) interactions whose rate Γ_{CET} of interaction varies as the inverse sixth power of both donor-acceptor separation distances (r_1, r_2):

$$\Gamma_{CET}(r_1, r_2) = \frac{Cte}{r_1^{-6} r_2^{-6}}. \qquad (3)$$

We aim at determining the role of rare earth concentration on cooperative energy transfer (*CET*) in rare earth ions solid solution in two kinds of thin films: (1) mixed *RE* thin film (2) multilayer thin film

constituted of an alternation of SiN_x:Yb^{3+} and SiN_x:Tb^{3+} sublayers of few nanometers thick. The influence of concentration of rare earth ions and [Tb]/[Yb] concentration ratio on donor (Tb^{3+}) acceptor (Yb^{3+}) separation distances is therefore investigated in this part. The inter-ions centers distance will be studied through the determination of (1) the average value and (2) nearest neighbor distances (r_1 = donor-acceptor1 and r_2 = donor-acceptor2), assuming a uniform rare earth ions distribution in mixed *RE* film and in tiny sublayer of the multilayer structure. This study has been realized by means of a Monte Carlo approach that distributes uniformly the ion positions in calculation boxes. Two kinds of calculating boxes were defined in order to study rare earth ions distribution in mixed *RE* and multilayer cases. Those two modeling boxes were used for various concentrations of *RE* in order to explore the role of concentration on average distances between ions. The ergodic hypothesis that statistical values obtained on a larger box is equivalent to the statistic obtained on many small boxes was verified. Consequently, for each calculation, the control of the number of boxes on which statistical studies were performed allows to reduce and keep constant the uncertainty of averaged values obtained.

Luminescence concentration quenching phenomena[39] appears whenever rare earth atoms are close enough to start to aggregate and to form clusters. Therefore, we first investigated the effect of a single *RE* concentration on first $<r_1>$ neighbor average distance. The power law decrease of $<r_1>$ (first nearest neighbor average distance) with respect to concentration retrieved within our simulations shows that this distance reaches the Tb diameters of about 0.35 nm[46] for concentrations about 2×10^{21} atoms·cm^{-3}. Note that the same result is obtained for Yb. Consequently, in the following, we will consider that an efficient *CET* avoiding concentration quenching is possible if the first neighbor average distance ($<r_1>$) remains greater than the Tb and Yb atomic diameters.

We then investigated a system containing Tb^{3+} and Yb^{3+} ions. The concentration ratio has been fixed to $[Yb^{3+}] = 2[Tb^{3+}]$ in mixed *RE* and multilayer films. This ratio value corresponds to the ideal case of an optimized down-conversion layer. For the *ML* structure, three configurations of sublayer thicknesses t_{Tb}/t_{Yb} have been studied, ie, 1/1 nm,

2/2 nm, and 3/3 nm. We have investigated the effect of increasing concentration on the first $<r_1>$ and second $<r_2>$ neighbor average distances (Figure 6A,B). The calculations have evidenced a power law decrease of $<r_1>$ and $<r_2>$ with increase of both RE ion concentrations in all cases. However, in the case of mixed RE film, $<r_1>$ and $<r_2>$ reach the RE atomic diameter for Tb concentration over 1×10^{21} atoms·cm^{-3} (Yb concentration below 2×10^{21} atoms·cm^{-3}) while for multilayer structures these distances remain above this threshold level. Moreover, the smaller the sublayer thicknesses t_{Tb}/t_{Yb}, the smaller the $<r_1>$ and $<r_2>$ values. Note that they anyway remain larger than the atomic diameter threshold value. For Tb concentration above 1×10^{21} atoms·cm^{-3} and in opposition to mixed RE film structure, the multilayer approach therefore prevents aggregation of RE Tb^{3+} and Yb^{3+} ions, which is detrimental for the emission properties.

Finally, we have investigated the first $<r_1>$ and second $<r_2>$ neighbor average distance in a two rare earth Tb^{3+} and Yb^{3+} ions systems with various concentration ranging from 3×10^{19} to 2×10^{21} cm^{-3} in mixed RE and multilayer films. For this latter, sublayer thicknesses t_{Tb}/t_{Yb} have been fixed to 1.5/1.5 nm, in accordance with the optimized structure we have grown. Because second neighbor average distance is evolving in the same manner as first neighbor average distance, we only present the latter on Figure 6C,D. In both cases, mixed RE and ML films, the distance $<r_1>$ remains constant with Tb^{3+} concentration and increases with ytterbium Yb^{3+} one. Despite the same concentration range, the $<r_1>$ values reached in mixed RE film remain smaller than those obtained for ML film. As aforementioned in formula ((1)), the PL intensity is a function of excited population N^*, which depend on pumping conditions and on both RE populations (terbium and ytterbium). Therefore, to promote strong PL two conditions need to be simultaneously realized (1) a large excitability of the matrix: Tb^{3+} system and (2) and the shorter distance between donor (Tb^{3+}) and acceptor (Yb^{3+}). Despite mixed RE films allow to reach shorter donor-acceptor distances, it results in high concentration regime to clusterization/aggregation of rare earth ions, which will quench the PL. On the contrary, ML structure allows the decrease of the donor-acceptor distance by tuning both concentration and sublayer thickness. Furthermore, it prevents too short inter-ions centers distances at which aggregation occurs. And finally, because the high concentration regime is only reached for one species in each sublayer, the resulting disorder created in the host matrix is lower than in the case of the mixed RE approach that incorporate both ions in the same time. The multilayer approach is therefore a way to incorporate more RE ions and to tune the interaction distances while controlling PL quenching phenomena. This modeling explains the larger PL observed for multilayers than for mixed RE films.

3.7 | Solar cell device

Now that the DC multilayer structure has been optimized, the goal is to study the effect of such DC layer on a solar cell. For this purpose, the fabrication steps, ie, deposition and post annealing treatment, have been integrated in an industrial cell fabrication process. The process flow of monolithic c-Si solar cells topped with DC layer has been previously described elsewhere[33] and is schematically presented in
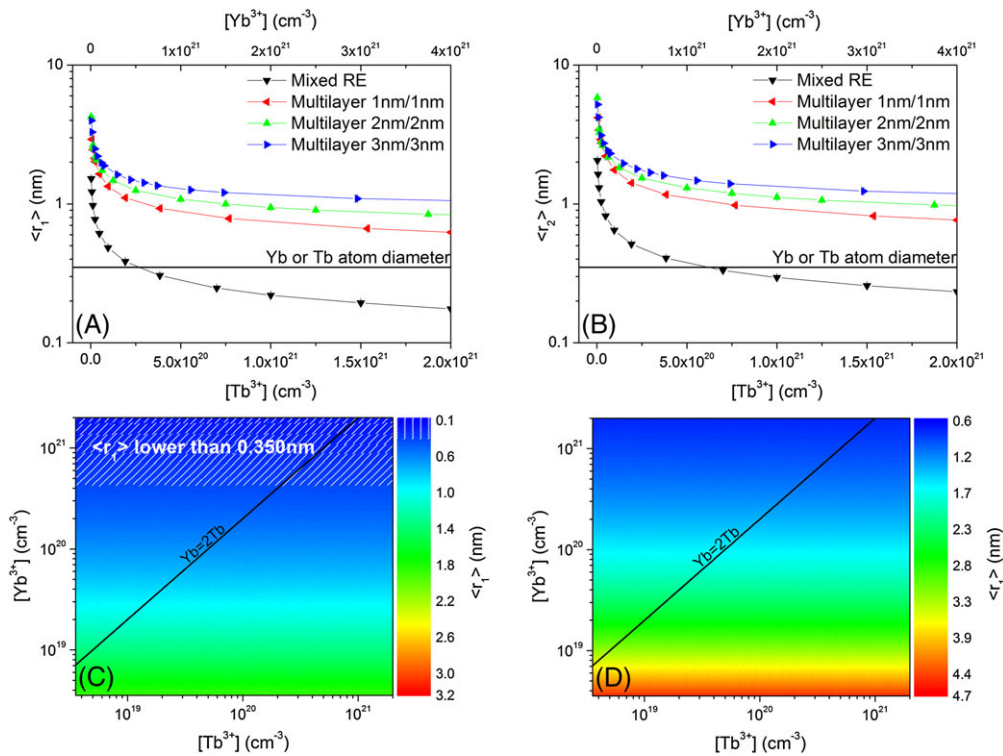

FIGURE 6 (A) First neighbor average distance $<r_1>$ and (B) second neighbor average distance $<r_2>$ between Tb^{3+} and Yb^{3+} ions as a function of Tb^{3+} ions concentration in a mixed RE-layer and multilayer film with uniform distribution for an ideal concentration of two Yb^{3+} for one Tb^{3+}. C, First neighbor average distance as a function of both RE ions concentrations in a mixed RE film with uniform distribution. The white dashed area represents $<r_1>$ below the diameter of Tb and Yb atoms equal to 0.35 nm. D, First neighbor average distance as a function of both RE ions concentrations in a multilayer film with uniform distribution [Colour figure can be viewed at wileyonlinelibrary.com]
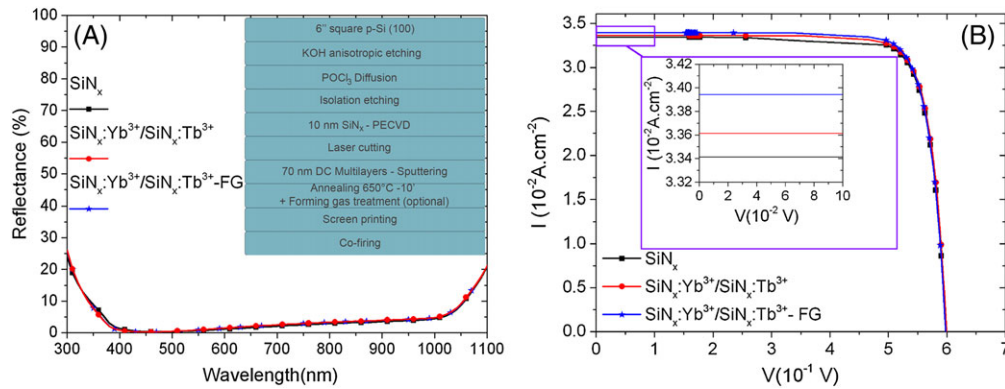
FIGURE 7 A, Reflectance of three layers (SiN_x, SiN_x:Yb^{3+}/SiN_x:Tb^{3+} *MLs*, SiN_x:Yb^{3+}/SiN_x:Tb^{3+} *MLs* with forming gas post treatment) deposited on textured emitters. B, *I-V* curves corrected of series resistance for three c-Si solar cells topped with SiN_x, SiN_x:Yb^{3+}/SiN_x:Tb^{3+} *MLs* and SiN_x:Yb^{3+}/SiN_x:Tb^{3+} *MLs* with forming gas post treatment [Colour figure can be viewed at wileyonlinelibrary.com]

inset of Figure 7. To fit the requirement of *DC* multilayer deposition due to the chamber geometry, samples needed to be cut into pieces. The SiN_x and SiN_x:Yb^{3+}/SiN_x:Tb^{3+} thin films were then deposited by cosputtering at 200°C and followed by an annealing process at 650°C during 10 min, as mentioned in Section 3.3.3. Note that to keep the standard industrial fabrication process in order to get the 80-nm-thick antireflective coating (*ARC*) layer for the Si-*SC*, the sputtered film should be 70-nm thick (total thickness of the *ARC* as 80 nm) and has a refractive index around 2.04 at 1.95 eV. For one of the devices, an added annealing treatment at 450°C during 30 min in forming gas (*FG*) has been carried out as such a treatment is known to recover some of the defects present in a layer, for example, dangling bonds. The deposition parameters and thickness control have been mentioned in the previous sections. Finally, the metallization of c-Si solar cells included the screen-printing and co-firing of Ag for the front contact and Al for the back contact. The process is summarized in the inset of Figure 7A.

The reflectivity of the fabricated *SC* is shown in Figure 7A. A minimum reflectance is observed at approximately 500 nm for the three solar cells, and the weight average reflectance (*WAR*) at *AM1.5G* in the range of 300 to 1200 nm is 5.68%. Such a result is the signature of a good light harvest of c-Si solar cell toped with *DC* multilayers. Because the metallization process of c-Si solar cells with *DC* layers was not optimized, the contact resistance was very high and the *SC* efficiency was lower than 5%. To overcome the series resistance influence and demonstrate the existence of an effect of the frequency conversion layer, Sinton's *Suns-V_{oc}* measurements have been performed.[47] External quantum efficiency (*EQE*) measurements have been carried out to deduce the short-circuit current density (*J_{sc}*). The resulting *I-V* curves corrected of series resistance are reported in Figure 7B. The c-Si solar cells with *DC* multilayers have higher efficiency than the one with SiN_x. Considering that the optical characteristics of the different structures studied are the same, we assume that this is a signature of a down-conversion effect. Moreover, the added annealing process in forming gas confirms such effect because the low temperature and short time annealing will not modify the antireflective properties but only allow the recovering of the nonradiative defects. As shown in Figure 7B and by the deduced photovoltaic performances reported in the Table 1, such a post annealing treatment

TABLE 1 Photovoltaic performances of c-Si solar cells with SiN_x, SiN_x:Yb^{3+}/SiN_x:Tb^{3+} multilayers structure annealed at 650°C-10 min, and SiN_x:Yb^{3+}/SiN_x:Tb^{3+} multilayers structure annealed at 650°C-10 min followed by a post treatment in forming gas (*FG*) at 450°C during 10 min. Pseudo means corrected of series resistance

ARC Layer	V_{oc}, V	J_{sc}, mA·cm^{-2}	Pseudo FF	Pseudo Efficiency (%) ± 0.03%
SiN_x	0.605	33.41	0.82	16.48
XC25(1.5/1.5)	0.599	33.61	0.82	16.53
XC25(1.5/1.5) + FG	0.598	33.94	0.82	16.66

improves the performance of c-Si solar cells. The comparison of the values reported in this table evidences an enhancement of the short-circuit current density (*J_{sc}*) and of the open-circuit voltage (*V_{oc}*) when a *DC* layer is present. The conversion efficiency corrected of the series resistance increases from 16.48% to 16.53% and 16.66% after a post-treatment in forming gas. This is to our knowledge the first time that the effect of a down-converter layer deposited on an industrial Monolithic c-Si solar cell is evidenced. These results are promising and demonstrate the potentiality of using a *DC* layer as an *ARC* one without modifying drastically the industrial process. Many issues concerning the passivation have anyway to be solved and several potential solutions are under studies.

4 | CONCLUSION

In this paper, we have detailed the fabrication process of a SiN_x-based multilayer structure doped with Tb^{3+} and Yb^{3+} ions for the development of efficient down-converter layer for Si solar cell. All the process described is fully compatible with the prerequisites of the *Si-PV* industry. The optimizations of the deposition parameters, such as the *RF* power density applied on rare earth targets, or the thicknesses of each sublayer have been carried out through the maximization of the *PL* emission of the Yb^{3+} ions. The performance of the optimized structure *XC25(1.5/1.5)* has been compared with the one of the best mixed *RE* SiN_x-Tb^{3+}:Yb^{3+} layer. An increase of the *PL* intensity by a factor 1.5 even with a lower Yb concentration in the multilayer structure is the demonstration of the key point played by the Tb-Yb interaction

distance in the cooperative energy transfer between Tb^{3+} and Yb^{3+} ions. The integration of the multilayer growth in the *Si-SC* industrial process flow has been performed and the characteristics of the *Si-SC* topped with such a *DC* have been studied. The bad efficiency recorded (lower than 5%) shows that the optimization of the *DC* layer deposition in the industrial process requires a specific attention. But the measurements performed using the method proposed by Kerr et al.[47] confirm the promising effect of using a frequency conversion layer on an industrial *Si-SC*. The development shown here is the demonstration of the feasibility of using frequency conversion layer compatible with the industry technology.

ORCID

Julien Cardin http://orcid.org/0000-0001-7069-4368
Didier Stiévenard http://orcid.org/0000-0003-2748-0254
Fabrice Gourbilleau http://orcid.org/0000-0003-3749-9178

REFERENCES

1. Yoshikawa K, Kawasaki H, Yoshida W, et al. Silicon heterojunction solar cell with interdigitated back contacts for a photoconversion efficiency over 26%. *Nat Energy*. 2017;2(5):17032.

2. Strumpel C, McCann M, Beaucarne G, et al. Modifying the solar spectrum to enhance silicon solar cell efficiency—an overview of available materials. *Sol Energy Mater Sol Cells*. 2006;91:238-249.

3. Radziemska E, Klugmann E. Thermally affected parameters of the current-voltage characteristics of silicon photocell. *Energ Conver Manage*. 2002;43(14):1889-1900.

4. Radziemska E. The effect of temperature on the power drop in crystalline silicon solar cells. *Renew Energy*. 2003;28(1):1-12.

5. Singh P, Singh S, Lal M, Husain MH. Temperature dependence of I-V characteristics and performance parameters of silicon solar cell. *Sol Energy Mater Sol Cells*. 2008;92(12):1611-1616.

6. Green MA, Bremner SP. Energy conversion approaches and materials for high-efficency photovoltaics. *Nat Mater*. 2017;16(1):23-34.

7. Lee Y, Dao VA, Iftiquar SM, Kim S, Yi J. Current transport studied of amorphous n/p junctions and its application in a-Si:H/HIT-type tandem cells. *Prog Photovolt Res Appl*. 2015;24:52-58.

8. Schnabel M, Canino M, Schilinger K, et al. Monolithic Si nanocrystal/crystalline Si tandem cells involving Si nanocrystals in SiC. *Prog Photovolt Res Appl*. 2016;24(9):1165-1177.

9. Yablonovitch E, Cody GD. Intensity enhancement in textured optical sheets. *IEEE Trans Electron Devices*. 1982;29(2):300-305.

10. Sai H, Kanomori Y, Arafune K, Ohshita Y, Yamaguchi M. Light trapping effect of submicron surface textures in crystalline Si solar cells. *Prog Photovolt Res Appl*. 2007;15(5):415-423.

11. Zhao J, Green M. Optimized antireflection coatings for high-efficiency silicon solar cells. *IEEE Trans Electron Devices*. 1991;38(8):1925-1934.

12. Bouhafs D, Moussi A, Chikouche A, Ruiz JM. Design and simulation of antireflection coating systems for optoelectronic devices: applications to silicon solar cells. *Sol Energy Mater Sol Cells*. 1998;52(1-2):79-93.

13. Cid M, Stem N, Brunetti C, Beloto AF, Ramos CAS. Improvements in anti-reflection coating for high-efficiency silicon solar cells. *Surf Coat Technol*. 1998;106(2-3):117-120.

14. Oskam KD, Wegh RT, Donker H, Loef EVD, van Meijerink A. Downconversion: a new route to visible quantum cutting. *J Alloys Compd*. 2000;300–301:421-425.

15. Richards BS. Luminescent layers for enhanced silicon solar cell performance: down-conversion. *Sol Energy Mater Sol Cells*. 2006;90(9):1189-1207.

16. Richards BS. Enhancing the performance of silicon solar cells via the application of passive luminescence conversion layers. *Sol Energy Mater Sol Cells*. 2006;90(15):2329-2337.

17. de la Mora MB, Amelines-Sarria Q, Monroy BM, Hernandez-Perez CD, Lugo JE. Materials for downconversion in solar cells: perspectives and challenges. *Sol Energy Mater Sol Cells*. 2017;165:59-71.

18. Trupke T, Shalav A, Richards BS, Wurfel P, Green MA. Efficiency enhancement of solar cells by luminescent up-conversion of sunlight. *Sol Energy Mater Sol Cells*. 2006;90(18-19):3327-3338.

19. Liu J, Yao Q, Li Y. Effects of downconversion luminescent film in dye-sensitized solar cells. *Appl Phys Lett*. 2006;88(17):173119.

20. Klampaftis E, Ross D, McIntosh KR, Richards BS. Enhancing the performance of silicon solar cells via the application of passive luminescence conversion layers. *Sol Energy Mater Sol Cells*. 2009;93(8):1182-1194.

21. Lakshminarayana G, Qiu J. Near-infrared quantum cutting in RE^{3+}/Yb^{3+} (RE=Pr, Tb, and Tm): GeO_2-B_2O_3-ZnO-LaF_3 glasses via downconversion. *J Alloys Compd*. 2009;481(1-2):582-589.

22. Ming C, Song F, An L, Ren X. Highly efficient quantum cutting in Yb/Pr-codoped $NaY(WO_4)_2$ crystal. *Curr Appl Phys*. 2014;14(8):1028-1030.

23. Xu YS, Huang F, Fan B, et al. Quantum cutting in Pr^{3+}-Yb^{3+} codoped chalcohalide glasses for high-efficiency c-Si solar cells. *Opt Lett*. 2014;39(8):2225-2228.

24. Vergeer P, Vlugt TJH, Kox MHF, den Hertog MI, van der Eerden JPJM, Meijerink A. Quantum cutting by cooperative energy transfer in Yb^{3+}. *Physical Rev B*. 2005;71(1):014119.

25. Cho E-C, Park S, Hao X, et al. Silicon quantum dot/crystalline silicon solar cells. *Nanotechnology*. 2008;19(24):245201.

26. Pan Z, Sekar G, Akrobetu R, Mu R, Morgan SH. Visible to near-infrared down-conversion luminescence in Tb^{3+} and Yb^{3+} co-doped lithium-lanthanum-aluminosilicate oxyfluoride glass and glass-ceramics. *J Non Cryst Solids*. 2012;358(15):1814-1817.

27. Rojas-Hernandez RE, Santos LF, Almeida RM. Tb^{3+}/Yb^{3+} doped aluminosilicate phosphors for near infrared emission and efficient downconversion. *JOL*. 2018;197:180-186.

28. Zhang Q, Wang J, Zhang G, Su Q. UV photon harvesting and enhanced near-infrared emission in novel quantum cutting Ca^{3+},Tb^{3+},Yb^{3+} phosphor. *J Mater Chem*. 2009;19(38):7088.

29. Lin H, Zhou S, Teng H, et al. Near infrared quantum cutting in heavy Yb doped $Ce_{0.03}Yb_{3x}Y_{(2.97-3x)}Al_5O_{12}$ transparent ceramics for crystalline silicon solar cells. *J Appl Phys*. 2010;107(4):043107.

30. Paschotta R, Nilsson J, Barber PR, Caplen JE, Tropper AC, Hanna DC. Lifetime quenching in Yb-doped fibres. *Opt Commun*. 1997;136(5-6):375-378.

31. An Y-T, Labbé C, Cardin J, Morales M, Gourbilleau F. Highly efficient infrared quantum cutting in Tb^{3+}–Yb^{3+} codoped silicon oxynitride for solar cell applications. *Adv Opt Mater*. 2013;1(11):855-862.

32. Dumont L, Cardin J, Benzo P, et al. SiN^{3+}-Yb^{3+}, an efficient down-conversion layer compatible with a silicon solar cell process. *Sol Energy Mater Sol Cells*. 2016;145:84-92.

33. Dumont L, Benzo P, Cardin J, et al. Down-shifting Si-based layer for Si solar applications. *Sol Energy Mater Sol Cells*. 2017;169:132-144.

34. Rabouw FT, Meijerink A. Modeling the cooperative energy transfer dynamics of quantum cutting for solar cells. *J Phys Chem C*. 2015;119:2364-2370.

35. Gourbilleau F, Madelon R, Dufour C, Rizk R. Fabrication and optical properties of Er-doped multilayers Si-rich SiO_2/SiO_2: size control, optimum Er–Si coupling and interaction distance monitoring. *Opt Mater*. 2005;27(5):868-875.

36. Debieu O, Nalini RP, Cardin J, Portier X, Perrière J, Gourbilleau F. Structural and optical characterization of pure Si-rich nitride thin films. *Nanoscale Res Lett*. 2013;8(1):31.

37. Forouhi AR, Bloomer I. Optical dispersion relations for amorphous semiconductors and amorphous dielectrics. *Phys Rev B*. 1986;34(10):7018-7026.

38. Jeong H, Seo S-Y, Shin JH. Excitation mechanism of visible, Tb^{3+} photoluminescence from Tb-doped silicon oxynitride. *Appl Phys Lett*. 2006;88(16):161910.

39. Auzel F. Upconversion and anti-stokes processes with f and d ions in solids. *Chem Rev*. 2004;104(1):139-173.

40. Labbé C, An YT, Zatryb G, et al. Structural and emission properties of Tb^{3+}-doped nitrogen-rich silicon oxynitride films. *Nanotechnology*. 2017;28(11):115710.

41. Bustarret E, Bensouda M, Habrard MC, Bruyère JC, Poulin S, Gujrathi SC. Configurational statistics in a-$Si_xN_yH_z$ alloys: a quantitative bonding analysis. *Phys Rev B*. 1998;38:8171.

42. Makino T. Composition and structure control by source gas ratio in LPCVD SiN_x. *Electrochem Soc*. 1983;130(2):450-455.

43. Kirkla EJ, Loane RF, Silcox J. simulation of annular dark field stem images using a modified multislice method. *Ultramicroscopy*. 1987;23:77.

44. Pennycook SJ. Z-contrast stem for materials science. *Ultramicroscopy*. 1989;58.

45. Navarro-Urrios D, Lebour Y, Jambois O, et al. Optically active Er^{3+} ions in SiO_2 codoped with Si nanoclusters. *J Appl Phys*. 2009;106(9):093107.

46. Slater JC. Atomic radii in crystals. *J Chem Phys*. 1964;41(10):3199-3204.

47. Kerr MJ, Cuevas A, Sinton RA. Generalized analysis of quasi-steady-state and transient decay open circuit voltage measurements. *J Appl Phys*. 2002;91(1):399-404.